Bol. Soc. Paran. Mat.
©SPM – E-ISSN-2175-1188
SPM: www.spm.uem.br/bspm

(3s.) **v. 2026 (44) 18** : 1–19.
ISSN-0037-8712
doi:10.5269/bspm.83224

Studying The Effects of Vertical-Horizontal Grooves on the (T-S) instabilities of Thermo-Viscous Flows Over a Heated Rough Plate

Mushrifah A. S. Al-Malki

ABSTRACT: The present paper studies the effects of flow and the stability behavior of an external boundary layer flow on the wave surface of a heated plate for a fluid. In addition to the effect of roughness, we took into account the temperature-dependent viscosity of the fluid. The grooved wall in a wavelike form is applied to the flow by modifying the no-penetration conditions on a heated plate. Our results indicate that increasing both temperature sensitivity, and the height of grooves acts to move the velocity and temperature profiles toward the plate surface with Liquid-type viscosities. Whereas gas-type viscosities act to show the reverse effect with decreasing both the height of the rough surface and temperature dependence. We then numerically examined impact on the linear stability and found that increasing the depth of wave-like grooves enhances the flow stability. This investigation is confirmed by a sharply reduction in the total energy contributions. This study may contribute to many applications in engineering and industrial fields.

Keywords: Stability, (T-S) Waves, vertical grooves, horizontal grooves, Hight Roughness.

Contents

1. Introduction

Since the mid- nineteenth century, there have been experimental studies testing examining the effects of turbulent flow on rough surface. Mansur et al. [1] experimentally tested a flow over a flat plate with semicircular rough surfaces for Reynolds numbers up to 2500, and this type of roughness is similar waviness. The results of this study indicate that the semicircular roughness acts to continue appearance of Reynolds curves without discontinuous. The numerical studies of Okajima [2], Lindquist et al. [3] and [4] showed the similar results for the discontinuities of the Strouhal number from their experiments on square rectangular cylinders. Hoph [5] found two types of different rough surfaces, which are related to the friction factor. One of them was named 'roughness of wall' with short wavelength and relatively high amplitude. A second type of roughness is named a "waviness wall", which is a long wavelength. Previous experimental data presented that the friction coefficient (f) is nearly independent of the Reynolds number (Re), but is very dependent on the relative roughness. The friction factor for wavy surfaces can be compared to that of a smooth tube. For more detailed historical context on the study of flow over rough surfaces, see Saleh's thesis [6]. In 1933, Nikuradse [7] conducted studies on the flow in internally rough

---

2020 *Mathematics Subject Classification:* 76D10, 76E15.
Submitted April 03, 2026. Published June 23, 2026.

pipes . This research is foundational in understanding how roughness affects fluid dynamics in pipes, influencing the design and analysis of various engineering systems involving fluid flow (see Nikuradse [8]).

In 1939, Colebrook [9] proposed the "universal" formula for calculating pressure loss in industrial tubes. This formula, known as the Colebrook equation, is a key tool to predict the friction factor in turbulent flow within rough pipes. The pioneering work of Nikuradse [7] in the 1930s laid the groundwork for this formula. He investigated flow in pipes with known roughness, which informed the development of the Moody diagram in 1944 [10]. The Moody diagram provides a graphical representation of the friction factor as a function of Reynolds number and relative roughness for various flow conditions.

According to Jiménez [11], and Perry et al. [12] made significant observations in their study of boundary layers over flat plates with narrow square grooves. Their findings lead to the distinction between D-roughness and K-roughness: The effective roughness of D-Roughness is proportional to the thickness of the boundary layer rather than the height of the roughness. This suggests that the thickness of the boundary layer plays a significant role in determining the flow characteristics on these surfaces. However, K-Roughness (or Normal Roughness) is directly proportional to the roughness dimensions. This type of roughness is typically referred to as "normal" roughness, and viscosity becomes irrelevant. Later, Schultz [13] and Flack [14] conducted detailed experiments comparing K-type and D-type roughness, highlighting differences in turbulent intensity and drag. Squire et al. [15], simulating urban-like roughness, demonstrated that at high Reynolds numbers, classical turbulence scaling laws often break down.

Rough surfaces are generally efficient generators of friction. However, this is not always the case, as some moderately rough surfaces can actually reduce drag, for an example of this is the flow over riblets, where a decrease in drag of up to 10 percent, has been observed by Sareen [16]. Bhaganagar and Kim [17], combining wind tunnel experiments and Direct Numerical Simulation (DNS), observed increased energy production and dissipation near roughness elements.

There is considerable engineering interest in the study of turbulent boundary layers over rough surfaces, especially at moderate Reynolds numbers. This interest is driven by the potential to optimize flow characteristics in various applications, such as improving fuel efficiency in transportation or enhancing heat transfer in cooling systems. Understanding the influence of surface roughness on turbulent boundary layers can lead to more efficient designs and better performance in numerous engineering systems. The ongoing research and experimental studies aim to improve the understanding of these complex interactions, ultimately leading to more efficient designs and processes in engineering applications. Molki et al. [18].

Miklavcic and Wang [19] developed a new model (MW) due to a rough rotating disk. Generally, this model is based on the creation of grooves on the disk such as concentric grooves or radial grooves in the radial and azimuthal directions, respectively.

The results of this study may also be applicable to the special case of a randomly rough disk. The investigation aims to understand how these roughness patterns affect the flow dynamics, including flow characteristics, examining how the opposite directions of roughness patterns such as uniform grooves influence the overall flow behavior around any surface. Furthermore, This study analyzed the impact of roughness on pressure drop and velocities distribution in the flow, and investigated the formation and behavior of turbulent flow structures near the rough surface of the disk. This study has broader implications for more applications, where rotating disks are used, particularly in engineering systems and surface roughness can affect performance [20], [21], [22]. From these the investigations, we will visualize that a flat plate is grooved by wavy roughness in vertical or horizontal direction, and this change will be named (anisotropic grooves). This roughness must be in opposite flow direction as known that the flow over a 2D-dimensional plate is only in one way, either in the x- or y-direction. Therefore, We will apply the model (MW) on a heated surface.

The Blasius boundary layer has been a fundamental topic in fluid mechanics since the early twentieth century [23]. Initial studies on small disturbances in laminar flow over a flat plate were conducted by Tollmien and Schlichting [24], and [25], who identified the amplification of linear wave-like disturbances as the primary mechanism for unstable flows. Their work was crucial in determining the critical Reynolds number, which marks the transition point from laminar to turbulent flow. The existence of Tollmien-Schlichting (T-S) waves was later confirmed by Schubauer [26], who observed these waves for the first time in experiments conducted in a heavily damped wind tunnel.

There are many studies that collectively advance the understanding of non-parallel effects on stability and improve the accuracy of theoretical predictions relative to experimental observations. For example, Fasel and Konzelmann [27] provided direct numerical solutions to a fully non-parallel problem, highlighting inconsistencies across different studies in determining which nonparallel terms are significant. They stressed the importance of using solutions to the Orr-Sommerfeld equation [28] as a first approximation when extending to non-parallel theory [29].

Although linear stability analyses generally focus on modeling the initial phases of transitional flows, many studies have emphasized the significance of nonlinearity and non-normality in predicting the transition to turbulence and their influence on the development of primary instabilities [30] and [31]. The e^N analysis developed by van Ingen [32] integrates non-linearity into a linear framework by using linear amplification rates. This method aligns well with empirical data on transitional Reynolds numbers observed in experiments (see [33]).

Our paper aims to analyze how wall roughness affects the (T-S) instabilities of the external layer flow with taking into our consideration the effects resulting from the change in viscosity of a fluid (gas, liquid), that depends on the temperature. The common applications such as aerodynamic Surface Design, hypersonic and high-speed, turbomachinery and internal Flows, environmental and atmospheric modeling, and Chemical Vapor Deposition (CVD) reactors [34], etc. We see in the (CVD) where maintaining laminar flow is crucial for regular and cohesive film growth. Sharp temperature gradients in (CVD) reactors can lead to variations in fluid properties, necessitating a temperature-dependent viscosity model [35]. Building on Miller et al.'s initial analysis [36] of flow stability on a smooth flat plate, this study will extend this work by incorporating the effects of the waviness wall, which was experimentally shown by Mansour et al. [1], with partial slip as studied in MW model [19]. The difference between MW model and our model is the pervious approach has been applied on rotating geometries (disks, cones) in three-dimensions, while this paper will examine the same idea but on a non-rotating surface in tow-dimensions. Here, the grooves will form a short or long wave length and the flat plate will change to a wavy grooved plate, including the effect of the temperature-dependent viscosity, as examined by Miller et al. [36] and Al-Malki et al. [37]. This approach will help better understand how these factors influence flow stability in many applications such as (CVD) reactors.

The rest of the paper is structured as follows. The next section 2 details the formulation, covering the model setup, characteristics of the undisturbed flow, and the interpretations of the solutions . Sections 3 and 4 focus on linear stability and energy analyses for a rough heated plate, considering scenarios involving vertical or horizontal grooves. Section 5 concludes the study.

2. Mean Flow of a Heated Rough Plate

2.1. Formulation

Consider a heated semi-infinite plate with an incompressible fluid body with velocity $X = (u^*, v^*)$, where u^* and v^* are the velocities in the streamwise and plate-normal directions x^* and y^*, respectively. Here T^* is the temperature of the fluid, and the plate is heated to a fixed temperature T^*_∞. Figure 1 shows the structure of the model in Cartesian Coordinates. We obtained the following system from the Navier-Stokes equations by using the nondimensional variables of the system, which are defined as

$$\begin{aligned} \mathbf{X} &= X^*_\infty(u,v), \qquad & (x^*,y^*) &= L^*(x,y), \qquad & t^* &= (L^*/X^*_\infty)t, \\ p^* &= P^* X^{*2}_\infty p, \qquad & T^* - T^*_\infty &= T\triangle T^*, \qquad & \nu^* &= \nu/\triangle T^*. \end{aligned}$$

We assume that the surface plate is grooved vertically or horizontally as seen in Figures 2 and 3. The partial-slip conditions will take this form; x-direction form, horizontal grooves:

$$u(y=0) = m_s \rho \lambda u'(y=0), \tag{2.1}$$

or y-direction form, vertical grooves:

$$v(x=0) = m_s \rho \lambda v'(x=0), \tag{2.2}$$

where m_s are the corresponding slip coefficients and ρ represents the density of the fluid, and λ is the viscosity. This formulation is clarified in [19]. We reduced the momentum and continuity system derived

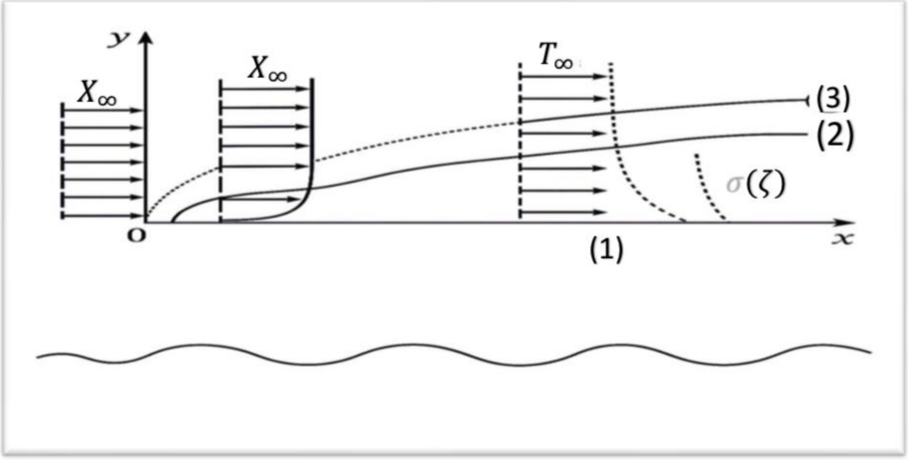

Figure 1: Visual schematic of the physical setup. (1) the grooved wall, (2) laminar/turbulent boundary layer, (3) thermally affected boundary region

from reference frame of Navier -Stokes equations to the ODE system. The establishment coordinate ζ, defined as $\zeta = x^{(-1)/2}y$. Then the following variables are selected for the transformation as follows:

$$u = h'(\zeta), \tag{2.3}$$

$$v = \frac{x^{(-1)/2}}{2}[\zeta h'(\zeta) - h(\zeta)]. \tag{2.4}$$

$$T = \Theta(\zeta). \tag{2.5}$$

We obtained the following equations.

$$(\bar{\lambda} h'')' + \frac{1}{2} h h'' = 0. \tag{2.6}$$

$$\Theta'' + \frac{1}{2} Pr h \Theta' = 0, \tag{2.7}$$

where the viscosity is based on the change of temperature, and is expressed by this form $\bar{\lambda} = (1 + \nu\Theta)^{-1}$. Pr is Prandtl number, which is determined in this study at the value $Pr = 0.72$, to be suitable for liquids and gases. The full formulation for above system can be seen in [37]. Equations 2.6 and 2.7 are the boundary value problem, which is solved using numerical methods, subject to the modified wall boundary conditions. Therefore, the grooved plate is represented by the partial-slip condition only in one direction ether x or y. This modification is considered because the fluid flow over a fat surface is only in one direction. The boundary conditions take the following form:

$$h(0) = 0, \quad u(0) = h'(0) = K_s h''(0), \quad \Theta(0) = 1 \tag{2.8}$$

and $h'(\zeta \to \infty) = 1$, $\Theta(\zeta \to \infty) \to 0$. Here, the primes denote differentiation regardingη, $K_s = m_s \rho \lambda$, gives experimental measures of the roughness only in one direction. This paper will present this type of roughness as horizontal or vertical grooves, as it is clear in Figures 2 and 3. These kinds of rough plates are like waves. These boundary conditions change to the non-penetration boundary conditions for a smooth plate, when $K_s = 0$. The solutions converge at $\zeta = 20$ to a tolerance of 10^{-8}; we consider this numerical representation of free-stream conditions $\zeta \to \infty$. The effect of ν on the boundary layer thickness σ^* is noted by measuring the Blasius constant δ, given by

$$\sigma = \int_0^\infty (1 - X) d\zeta = \sigma^* \sqrt{\frac{\rho^* X^*_\infty}{\lambda^*_\infty x^*}}. \tag{2.9}$$

Figure 2: Horizontal grooves.

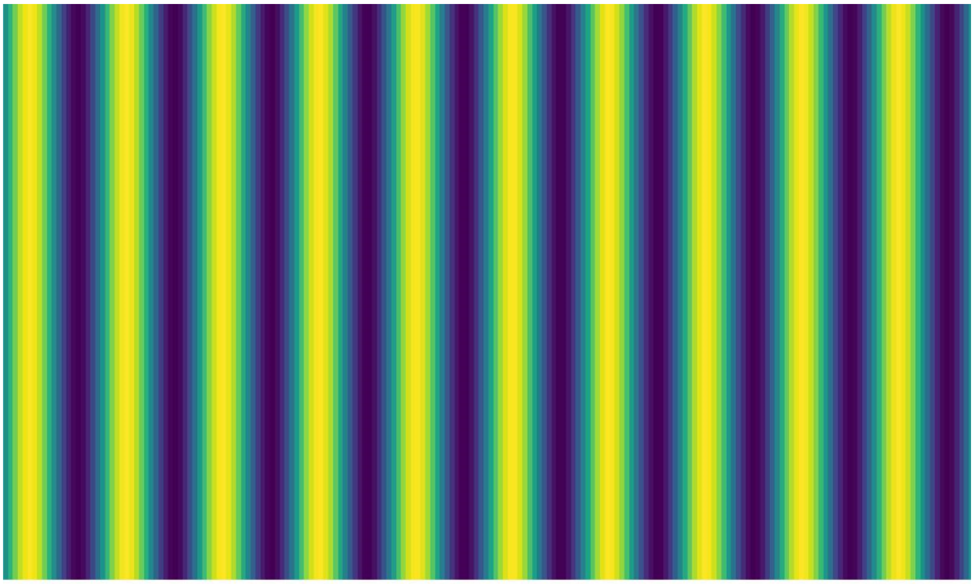

Figure 3: Vertical Grooves.

2.2. The solutions For The Mean System

The equations (2.6-2.9) are solved by the (bvp4c) Method using Matlab language The plots in Figure 4 clarify the influence of the vertical roughness, and the combined grooves with higher temperatures of the fluid (gas-liquid). The curves move close to the surface, as we use greater values for both grooves and temperature. The boundary layers are very thin specially the red curves, which show the viscosity in the liquid case. The uniform viscosity is denoted by $\lambda(\zeta) = 1$ (green line). Here, the viscosity remained constant despite the increase in surface roughness.

Figure 5 displays a good comparison between each case of the fluid from gases to liquids. In this figures, the mean flow velocities are presented by $X(\zeta)$, $X'(\zeta)$, and $\Theta(\zeta)$, where the flow velocities were plotted for three cases of temperature-dependent viscosity with increasing the hight of grooves of the surface from 0 to 1 (increment 0.25). In all outer boundary layer profiles: blue represents gas flow with temperature-dependent viscosity ($\nu = -0.75$), green corresponds to the case of constant viscosity at zero temperature ($\nu = 0$), and red indicates liquid-phase flow at elevated temperature with lower viscosity ($\nu = 0.75$).

Figure 5 (a) displays the profiles of the $X(\zeta)$. The blue curves at fixed $\nu = -0.75$ and increasing K_s show the behavior of the boundary layer in fluid flow over a flat plate, where the velocity profiles gradually form, starting from zero at the surface and increasing up to (0.1). We note that the velocity increases progressively with distance close to the plate. At zero temperature and a gradual increase in the depth of the roughness (K_s), the green velocity profiles become closer to the surface and show higher velocity values. But the boundary layers are thicker and the fluid accelerates faster as noted in Table 1, likely due to lower viscosity at this value of the temperature, and uniform surface grooves cause a slip velocity near the wall by allowing fluid to partially enter the grooves. This reduces friction, modifies the boundary layer, and leads to faster flow near the surface compared to a smooth wall. When ν equals 0.75 with the same range of the K_s values, we observe the similar changes that seen in green plots but the red profiles are closer to the plate and greater slip velocity, making the flow faster than from previous cases. We notice that the lower viscosity and the deeper roughness lead to moving the velocities to the surface. It is clear that all profiles appear nearly parallel and the boundary layer thickness is almost constant at the surface while it is thinner as $X(\zeta)$ reaches one away from the plate to free stream, this indicates that the flow has become steady and uniform (laminar).

Similarity, Figures 5 (b) and (c) of the $X'(\zeta)$ and the $\Theta(\zeta)$ have the same changes that seen in Figures 5 (a). This reflects the natural development of the boundary layer along the plate are less disturbance or separation.

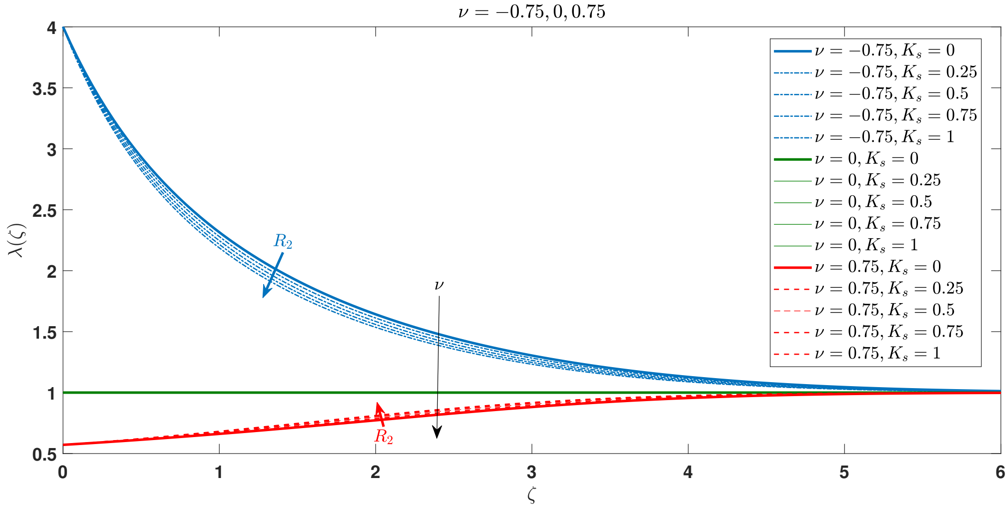

Figure 4: The viscosity profiles $\bar{\lambda}(\zeta)$ for a range of roughness $K_s > 0$.

3. Stability of the Linearized System

3.1. Deriving the equations for perturbations

Minor disturbances are now actively altering the mean-flow solutions, giving rise to

$$U(x,y,t) = u(x,y) + \hat{U}(x,y,t), \tag{3.1}$$

$$V(x,y,t) = R^{(\frac{-1}{2})} v(x,y) + \hat{V}(x,y,t), \tag{3.2}$$

$$P(x,y,t) = p(x) + \hat{P}(x,y,t), \tag{3.3}$$

$$T(x,y,t) = \Theta(x,y) + \hat{\theta}(x,y,t). \tag{3.4}$$

The governing equations have been reformulated in a dimensionless form, incorporating new characteristic scales for length, velocity, time, pressure, and temperature which determine the resulting coefficients:

$$X^* = X^*_\infty \left(U, V\right), \qquad (x^*, y^*) = \sigma^*(x,y), \qquad t^* = \left(\sigma^*/X^*_\infty\right) t,$$

$$p^* = \rho^* {X^*_\infty}^2 p, \qquad T^* - T^*_\infty = T\sigma T^*, \qquad \nu^* = \nu/\sigma T^*.$$

Notably, the scaling method remains consistent, with the only differences being adjustments to the characteristic length and time scales, which are now derived from the boundary layer thickness σ^*. Consequently, the Reynolds number (Re) is redefined accordingly:

$$Re = \sigma\sqrt{xR}.$$

The modified base flow expressions from equations (3.1 - 3.4) are substituted into the resulting equation system. For analytical convenience, we adopt the "parallel flow approximation," which presumes that disturbances arise sufficiently far downstream $(x \gg 1)$, rendering the streamwise evolution of the boundary layer negligible. Under this assumption, the primary flow variables u and θ depend exclusively on the transverse coordinate y, while v is assumed to be significantly less than one. To maintain consistency with the base flow characteristics, the viscosity λ is approximated via a first-order Taylor expansion.

$$\lambda \approx \frac{1}{1+\nu\Theta} - \frac{\nu\hat{\Theta}}{\left(1+\nu\Theta\right)^2} = \bar{\lambda} + \hat{\lambda},$$

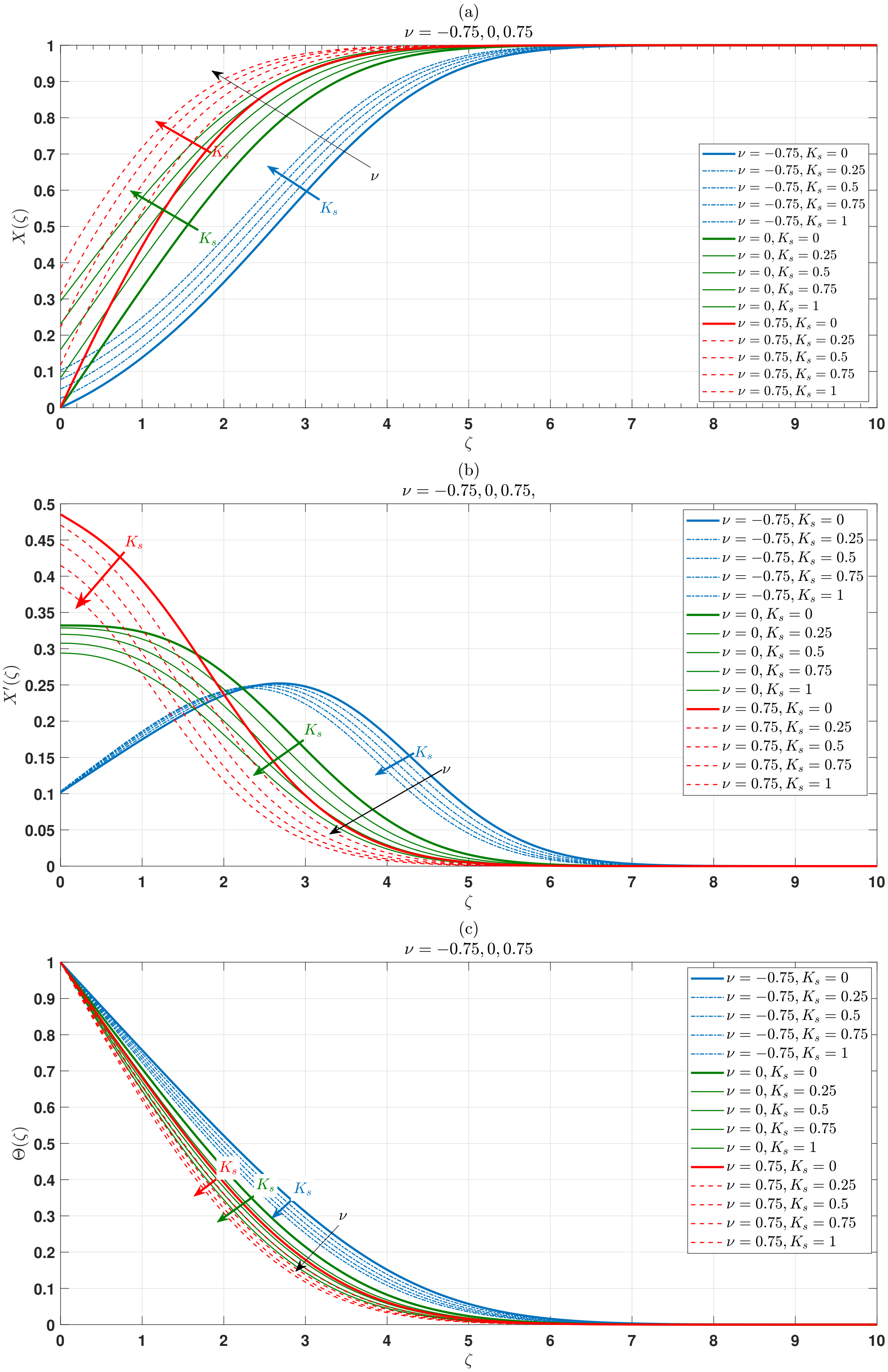

Figure 5: Mean flow profiles for a range of values roughness $K_s > 0$. (a) $X(\zeta)$ (streamwise profile), (b) $X'(\zeta)$ (velocity gradient), and (c) $\Theta(\zeta)$ (temperature).

Table 1: The mean flow data for a range of $K_s > 0$ (horizontal or vertical grooves) at fixed ν values.

$\nu = -0.75$		
K_s	$X(\zeta)$	$X'(\zeta)$
0	0	0.103317
0.25	0.0256186	0.103317
0.5	0.05152663	0.103317
0.75	0.082157	0.103317
1	0.103317	0.103317
$\nu = 0$		
K_s	$X(\zeta)$	$X'(\zeta)$
0	0	0.332057
0.25	0.082157	0.328628
0.5	0.159892	0.319784
0.75	0.236044	0.307645
1	0.293897	0.293876
$\nu = 0.75$		
K_s	$X(\zeta)$	$X'(\zeta)$
0	0	0.485333
0.25	0.117636	0.470545
0.5	0.222352	0.444704
0.75	0.311157	0.414878
1	0.385104	0.385104

Where $\hat{\lambda} = -\nu\bar{\lambda}^2\hat{\Theta}$. We now arrive at a system of partial differential equations that can be separated into components dependent on x and t.

$$\frac{\partial \hat{U}}{\partial x} + \frac{\partial \hat{V}}{\partial y} = 0, \tag{3.5}$$

$$\frac{\partial \hat{U}}{\partial t} + u\frac{\partial \hat{U}}{\partial x} + u'\hat{V} + \frac{\partial \hat{P}}{\partial x} = \frac{\bar{\lambda}}{Re}\left(\frac{\partial^2 \hat{U}}{\partial x^2} + \frac{\partial^2 \hat{U}}{\partial y^2}\right) + \frac{\bar{\lambda}'}{Re}\left(\frac{\partial \hat{V}}{\partial x} + \frac{\partial \hat{U}}{\partial y}\right) + \frac{u''\hat{\lambda}}{Re} + \frac{u'}{Re}\frac{\partial \hat{\lambda}}{\partial y}, \tag{3.6}$$

$$\frac{\partial \hat{V}}{\partial t} + u\frac{\partial \hat{V}}{\partial x} + \frac{\partial \hat{P}}{\partial y} = \frac{\bar{\lambda}}{Re}\left(\frac{\partial^2 \hat{V}}{\partial x^2} + \frac{\partial^2 \hat{V}}{\partial y^2}\right) + \frac{2\bar{\lambda}'}{Re}\frac{\partial \hat{V}}{\partial y} + \frac{u'}{Re}\frac{\partial \hat{\lambda}}{\partial x}, \tag{3.7}$$

$$\frac{\partial \hat{\theta}}{\partial t} + u\frac{\partial \hat{\theta}}{\partial x} + \theta'\hat{V} = \frac{1}{RePr}\left(\frac{\partial^2 \hat{\theta}}{\partial x^2} + \frac{\partial^2 \hat{\theta}}{\partial y^2}\right), \tag{3.8}$$

Perturbation variables are commonly expressed using a normal mode formulation

$$\left(\hat{U}, \hat{V}, \hat{P}, \hat{\theta}\right) = \left(\tilde{U}, \tilde{V}, \tilde{P}, \tilde{\theta}\right) e^{i(\alpha x - \omega t)}.$$

Where, α denotes the complex wavenumber in the streamwise direction, with α_r and α_i representing its real and imaginary components, respectively. The parameter ω corresponds to the real-valued disturbance frequency. A negative α_i indicates convective instability, implying that the disturbance amplifies as it moves downstream with the flow. The governing stability equations are obtained by substituting this normal mode representation into Equations (3.5–3.8) to express the perturbation fields.

$$i\alpha\tilde{U} + \tilde{V}' = 0, \tag{3.9}$$

$$i\left(\alpha u-\omega\right)\tilde{U}+u'\tilde{V}+i\alpha\tilde{P}=\frac{\bar{\lambda}}{Re}\left(\tilde{U}''-\alpha^2\tilde{U}\right)-\frac{\nu\bar{\lambda}^2}{Re}\left[\Theta'\left(\tilde{U}'+i\alpha\tilde{V}\right)+\left(\tilde{U}'\tilde{\theta}\right)'\right]+\frac{2\lambda^2\bar{\lambda}^3u'\Theta'\tilde{\theta}}{Re}, \quad (3.10)$$

$$i\left(\alpha u-\omega\right)\tilde{V}+\tilde{P}'=\frac{\bar{\lambda}}{Re}\left(\tilde{V}''-\alpha^2\tilde{V}\right)+\frac{\lambda\bar{\lambda}^2}{Re}\left[2\Theta'\tilde{V}'+i\alpha U'\tilde{\theta}\right], \quad (3.11)$$

$$i\left(\alpha u-\omega\right)\tilde{\theta}+\Theta'\tilde{V}=\frac{1}{RePr}\left(\tilde{\theta}''-\alpha^2\tilde{\theta}\right). \quad (3.12)$$

As ν tends toward zero, the formulation reduces to the classical fourth-order Orr–Sommerfeld equation. The problem of determining solutions for Equations (3.9–3.12) can be reformulated as a quadratic eigenvalue problem of the form:

$\left(M_2\alpha^2+M_1\alpha+M_0\right)\tilde{Q}=0$, where $\tilde{Q}$ stands for the vector consisting of eigenfunctions: $\left(\tilde{U},\tilde{V},\tilde{P},\tilde{\theta}\right)^T$. The matrices M_0, M_1, and M_2 hold the coefficients corresponding to the terms of order $\mathcal{O}\left(\alpha^0\right)$, $\mathcal{O}\left(\alpha^1\right)$, and $\mathcal{O}\left(\alpha^2\right)$,, in that order. The specified boundary conditions are applied to find the eigenfunctions:

$$\tilde{U}\left(0\right)=\tilde{V}\left(0\right)=\tilde{V}'\left(0\right)=\tilde{P}\left(0\right)=\tilde{\theta}\left(0\right)=0, \quad (3.13)$$

$$\tilde{U}\left(\infty\right)=\tilde{V}\left(\infty\right)=\tilde{P}\left(\infty\right)=\tilde{\theta}\left(\infty\right)\to 0. \quad (3.14)$$

The no-slip condition is imposed along the wall, with the boundary for $\tilde{v}'$ derived from Equation (3.9), while the plate is assumed to remain at a constant, fluctuation-free temperature. All perturbations are further required to decay to zero at sufficiently large distances from the surface. Neutral stability solutions in both temporal and spatial frameworks are obtained via Chebyshev polynomial discretization based on the our results that obtained from the mean flow solutions. The governing stability equations, expressed in primitive variables, are solved at 100 uniformly spaced collocation points spanning the domain from the lower to the upper boundary. Boundary conditions, as prescribed in Equations (3.13–3.14), are enforced at $y=0$ and $y=y_{max}$, where the mean flow reaches convergence at $y_{max}=20$.

3.2. Physical interpretation of the linear stability results

The above equations (3.9- 3.14) are numerically solved by Matlab language to find the relationship between the frequency $F=\frac{\omega}{Re}$, and the Reynolds number (Re). As known from previous studies, the area enclosed ($\alpha_i<0$) by neutral curves represented of this relationship is the unstable region while the outside ($\alpha_i>0$) of these curves is a stable area of the flow (T-S) waves.

Physically, we note in Figure 6 (a) that the neutral curves extremely close to each other, when we examine the gas ($\nu=-0.75$) case of the fluid ($\nu<o$) and increase the roughness depth. Although increasing the roughness depth raises the Reynolds number, this increase is very small in the case of gases. This means that the effect is still destabilizing, since the maximum groove depth is considered small. We expect that by taking larger roughness values, the Reynolds number will become higher. This trend in the values is beneficial and useful for increasing the stability of fluid flow.

In Figure 6 (b), when ν is raised to zero, the fluid viscosity becomes uniform; therefore, we notice that increasing K_s enhances stability to a greater extent, with viscosity remaining constant and independent of temperature. Compared to the previous case that seen in Figure 6 , the fluid flow is more stable. It is clear that roughness is a more effective factor with fluids that have constant viscosity, as the fluid partially slides over a uniformly rough surface resembling regular waves. This waviness contributes to stabilizing the fluid flow and also works to delay or dampen disturbances that destabilize the flow of the (T-S) waves.

At $\nu=0.75$ in Figure 6 (c) that shows that stability is greatly increased when both temperature and roughness are increased simultaneously. This means that fluid flow in the liquid state, with high temperature and high roughness, will be more stable than in all previous cases. This is very clear from the significant increase in the Reynolds number, which makes the unstable region smaller in area, as shown in the figure related to the explanation.

In general, uniform surface roughness increases the stability of fluid flow in all previous studies; therefore, our study is in strong agreement with the previous research regarding the effect of the roughness factor [21], [19], [20]. All our interpretations in this context are supported by critical value data, which are clearly presented in the attached Table 1.

Table 2: Critical data for a range of $K_s > 0$ (horizontal or vertical grooves) at fixed ν values.

$\nu = -0.75$			
K_s	Re_c	$F \times 10^6$	$\alpha_{r,c}$
0	150.07	2298.26	0.6512
0.25	155.17	2174.39	0.6254
0.5	160.15	2061.82	0.6006
0.75	164.98	1966.30	0.5788
1	169.62	1871.83	0.5561
$\nu = 0$			
K_s	Re_c	$F \times 10^6$	$\alpha_{r,c}$
0	519.08	232.72	0.3044
0.25	641.09	178.45	0.2648
0.5	755.70	145.69	0.2341
0.75	857.10	123.32	0.2081
1	944.20	107.82	0.1874
$\nu = 0.75$			
K_s	Re_c	$F \times 10^6$	$\alpha_{r,c}$
0	1124.80	61.88	0.2265
0.25	1449.40	49.95	0.1931
0.5	1743.90	41.46	0.1643
0.75	1910	38.17	0.1457
1	2054.40	4.41	0.1283

3.3. Eigen Functions

In the coming Section 4, energy balance study will employ Type I eigenfunctions, which here are evaluated at $Re = Re_c + 200$, $\nu = -0.75, 0, 2$, and a range of the K_s, a position well within the unstable range. The parameter α is chosen to correspond to the disturbance that experiences the greatest amplification at the specified Reynolds number.

From the Figure 7 (a) of the $|\tilde{U}|$ profiles, it is observed that at $\nu < 0$, the eigenvelocities, represented in blue, move away the surface, and the boundary layers are notably narrow and closely spaced. Furthermore, three distinct peaks are present, with the first peak on the right exhibiting a curvature. These peaks gradually increase in magnitude as the surface of the plate is approached. This indicates that the flow in this case is highly turbulent, although an increase in the value of K_s tends to mitigate this turbulence. This interpretation is consistent with the explanation of velocity behavior in the case of steady flow. In the same figure, at $\nu = 0$ the green and increasing K_s eigenfunctions profiles tend to approach the surface more prominently, and the two upper peaks that seen in blue curves merge into a single peak. In addition, a downward decrease in the jet is observed as K_s value is increased. The similar behavior is noted with the red eigenfunction curves at $\nu > 0$ and increasing K_s, but to a much greater extent, as is evident from the red curves in Figure 7 (a).

The curves in Figure 7 (b) of the $|\tilde{V}|$ perturbations, respectively, exhibit the same conduct with respect to the jet height reduction and the velocities approaching the surface of the flow profiles for three cases of the temperature (ν) (blue, green, and red), that observed in Figure 7 (a). It is observed that the changes in the eigenfunctions under turbulent flow conditions are consistent with, and dependent upon, the same variations observed in the primary flows.

As for the turbulent temperature profiles ($|\tilde{\theta}|$), we record an inverse trend as follows: the higher

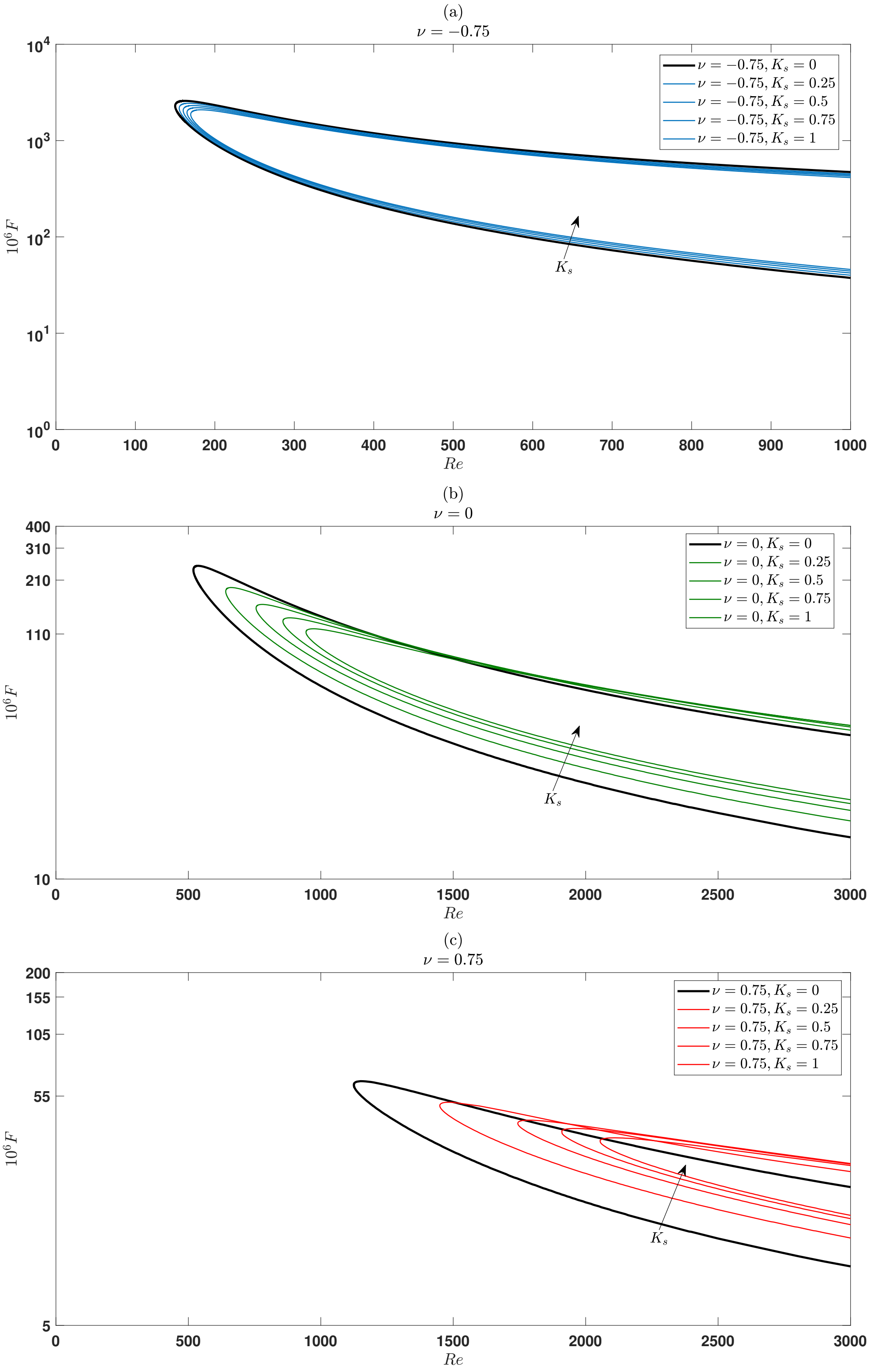

(a)
$\nu = -0.75$

(b)
$\nu = 0$

(c)
$\nu = 0.75$

Figure 6: Curves illustrating the transition point between stability and instability with changing viscosity ($\nu = -0.75, 0, 0.75$) and a range of grooves $K_s > 0$.

the temperature, the lower the profiles and the closer they are to the surface; whereas the greater the roughness depth, the higher the jet rises gradually as it is apparent in Figure 7 (c).

4. Energy Analysis

4.1. Formulation

Analyzing how disturbances contribute energy to or extract energy from the mean flow relies on the eigenfunctions. By multiplying equations 3.6 and 3.7 by $\hat{U}$ and $\hat{V}$, respectively, and then adding them together, one obtains an expression that describes the system's energy transfer mechanisms:

$$\begin{aligned}\hat{U}\frac{\partial \hat{U}}{\partial t}+\hat{V}\frac{\partial \hat{V}}{\partial t}+u\left(\hat{U}\frac{\partial \hat{U}}{\partial x}+\hat{V}\frac{\partial \hat{V}}{\partial x}\right)+u'\hat{U}\hat{V} &= -\left(\hat{U}\frac{\partial \hat{P}}{\partial x}+\hat{V}\frac{\partial \hat{P}}{\partial y}\right)\\ &+\frac{\bar{\lambda}}{Re}\left(\hat{U}\frac{\partial^2 \hat{U}}{\partial x^2}+\hat{U}\frac{\partial^2 \hat{V}}{\partial y^2}+\hat{V}\frac{\partial^2 \hat{V}}{\partial x^2}+\hat{V}\frac{\partial^2 \hat{U}}{\partial y^2}\right)\\ &+\frac{\bar{\lambda}'}{Re}\left(\hat{U}\frac{\partial \hat{V}}{\partial x}+\hat{U}\frac{\partial \hat{U}}{\partial y}+2\hat{V}\frac{\partial \hat{V}}{\partial y}\right)\\ &+\frac{u'}{Re}\left(\hat{U}\frac{\partial \hat{\lambda}}{\partial y}+\hat{V}\frac{\partial \hat{\lambda}}{\partial x}\right)+\frac{u''\hat{U}\hat{\lambda}}{Re}.\end{aligned} \tag{4.1}$$

The definitions of the variables provided below are as follows:

$$\hat{e_1}=\frac{1}{2}\left(\hat{U}^2+\hat{V}^2\right),\quad \hat{e_2}=\frac{\partial \hat{V}}{\partial x}-\frac{\partial \hat{U}}{\partial y},\quad \hat{e_3}=\frac{\partial \hat{V}}{\partial x}+\frac{\partial \hat{U}}{\partial y},$$

here, $\bar{e_1}$ represents the kinetic energy associated with the two disturbance variables, $\hat{e_2}$ denotes the disturbance vorticity, and $\hat{e_3}$ is introduced solely for notational convenience. After some algebraic rearrangement of expression (4.1), the energy equation can be written as:

$$\begin{aligned}\left(\frac{\partial}{\partial t}+u\frac{\partial}{\partial x}\right)\hat{e_1}+u'\hat{U}\hat{V} &= -\frac{\partial\left(\hat{U}\hat{P}\right)}{\partial x}-\frac{\partial\left(\hat{V}\hat{P}\right)}{\partial y}\\ +\frac{\bar{\lambda}}{Re}\left[\frac{\partial\left(\hat{V}\hat{e_2}\right)}{\partial x}-\frac{\partial\left(\hat{V}\hat{e_2}\right)}{\partial y}-\hat{e_2}^2\right] &+\frac{1}{Re}\left\{\bar{\lambda}'\left[\frac{\partial\left(\hat{U}\hat{V}\right)}{\partial x}\right.\right.\\ \left.+\frac{\partial\left(\hat{e_1}+\hat{V}^2\right)}{\partial y}\right] &+u'\left[\frac{\partial\left(\hat{\lambda}\hat{U}\right)}{\partial y}+\frac{\partial\left(\hat{\lambda}\hat{V}\right)}{\partial x}-\hat{\lambda}\hat{e_3}\right]\\ &\left.+u''\hat{\lambda}\hat{U}\right\}.\end{aligned} \tag{4.2}$$

By performing a full integration across the boundary layer, the energy equation is thoroughly obtained in the integral formulation given below:

$$\begin{aligned}\frac{dE}{dx} &= -\left\{\int_0^\infty u'\langle\hat{U}\hat{V}\rangle\,dy\right\}^A+\frac{1}{Re}\left\{\frac{d}{dx}\int_0^\infty \bar{\lambda}\langle\hat{V}\hat{e_2}\rangle\,dy-\int_0^\infty \bar{\mu}\langle\hat{e_2}^2\rangle\,dy\right\}^B\\ &+\frac{1}{Re}\left\{\frac{d}{dx}\int_0^\infty\left(\bar{\lambda}'\langle\hat{U}\hat{V}\rangle+u'\langle\hat{\lambda}\hat{V}\rangle\right)dy\right.\\ &\left.+\int_0^\infty\left(\bar{\lambda}'\langle\hat{U}\hat{e_2}\rangle-\bar{\lambda}''\left(\langle\hat{e_1}+\hat{V}^2\rangle\right)-u'\langle\hat{\lambda}\hat{e_3}\rangle\right)dy\right\}^C.\end{aligned} \tag{4.3}$$

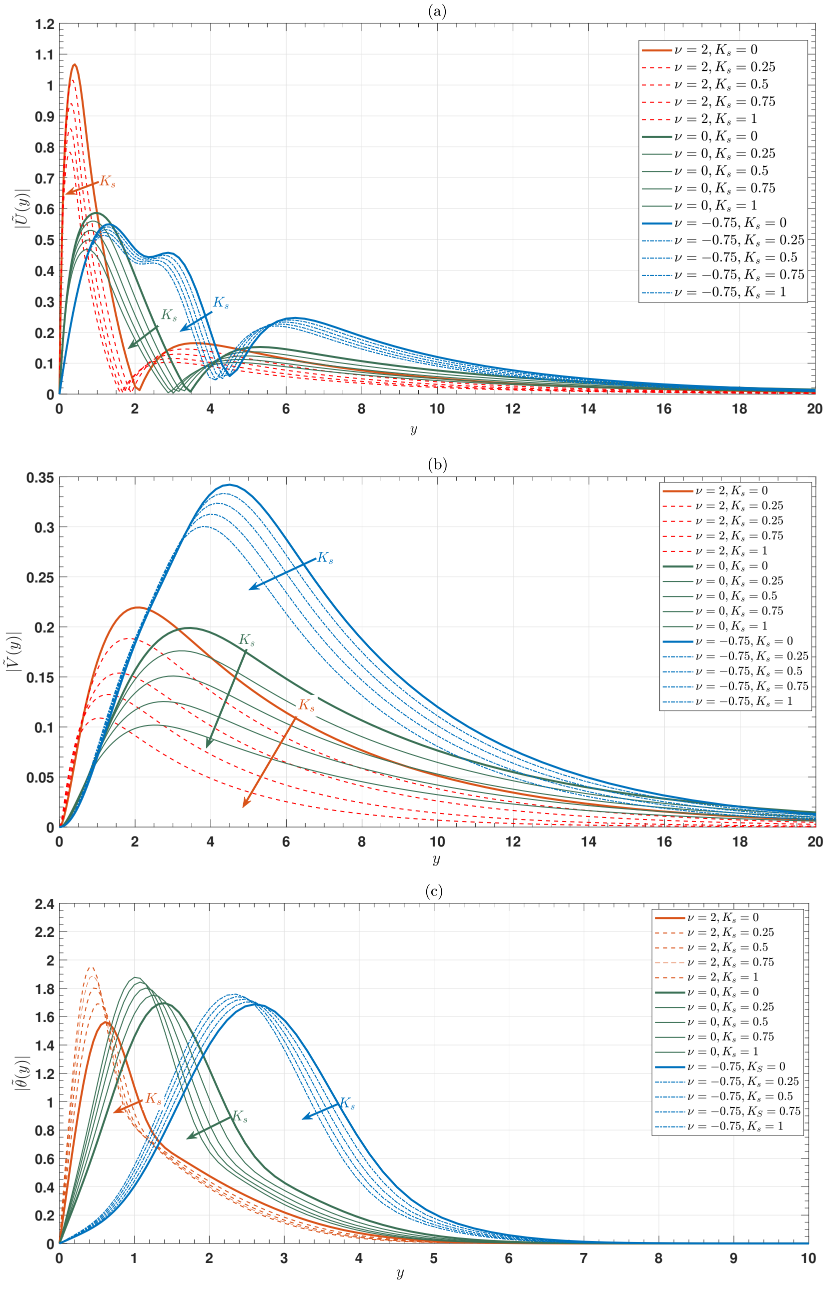

Figure 7: Perturbation eigenfunctions for $(\nu = -0.75, 0, 2)$ and a range of hight of grooves (K_s). (a) Streamwise Perturbation. (b) Plate normal perturbation. (c) Temperature Perturbation).

The quantities appearing on the left-hand side of equation (4.3) rigorously embody the system's total mechanical energy (E_{tm}), wherein: $E = \int_0^\infty \left(u\langle \hat{e_1}\rangle + \langle \hat{U}\hat{P}\rangle\right) dy$. Integral A constitutes a definitive measure of mechanical energy production attributable to Reynolds stress mechanisms (R_{ep}), while integral B represents the exact quantification of viscous-induced energy dissipation (V_{ed}). The terms collected in C emerge exclusively from spatial or temporal variability in viscosity (V_{av}) and identically annul in the inviscid limit, $\nu = 0$. The computational determination of the system's total mechanical energy (T_{me}) presents the predominant contributions on the left-hand side arise from term A and the second subcomponent of term B. The terms grouped under C are asymptotically negligible and are thus systematically excluded from the analysis. The remaining terms are subsequently normalized in exact accordance with: $\int_0^\infty \left(u\left\langle \tilde{e_1}\right\rangle + \left\langle \tilde{U}\tilde{P}\right\rangle\right) dy$, as provided below

$$\underbrace{-2\alpha_i}_{T_{me}} \approx \underbrace{\int_0^\infty \left\langle \tilde{U}\tilde{V}\right\rangle u' dy}_{R_{ep}} + \underbrace{\frac{1}{Re}\int_0^\infty \bar{\lambda}\left\langle \tilde{e_2}^2\right\rangle dy}_{V_{ed}}, \tag{4.4}$$

where $\tilde{e_1} = \frac{1}{2}\left(\tilde{U}^2 + \tilde{V}^2\right)$, $\tilde{e_2} = i\alpha\tilde{V} - \tilde{U}'$, and $\langle \tilde{x}\tilde{y}\rangle = \tilde{x}\tilde{y}^* + \tilde{x}^*\tilde{y}$. Here, * denotes the complex conjugate. Sustained amplification of a turbulent eigenmode arises only when the instantaneous rate of energy production unambiguously exceeds the total energy dissipated through viscous mechanisms. In the present formulation, the V_{ed} is rigorously decomposed into an invariant constant-viscosity contribution and a temperature-dependent term, thereby establishing:

$$\underbrace{\int_0^\infty \bar{\lambda}\left\langle \hat{e_2}^2\right\rangle dy}_{V_{ed}} = \underbrace{\int_0^\infty \left\langle \hat{e_2}^2\right\rangle dy}_{N_d} + \underbrace{\int_0^\infty \left(\bar{\lambda} - 1\right)\left\langle \hat{e_3}^2\right\rangle dy.}_{T_{dd}} \tag{4.5}$$

In this context, N_d denotes Newtonian dissipation, whereas T_{dd} signifies temperature-dependent dissipation. This decomposition within V_{ed} enables a deeper examination of the decisive role that variable viscosity plays in governing flow stability, particularly under increasing the grooves depth of the roughness and the temperature (ν).

4.2. Interpretation of the energy study results

The amplification occurs in a turbulent eigenmode once energy production predominates over dissipation. Figure 8(a) illustrates how the energy contributions vary under different combined roughness (K_s) intensity values with a range of the temperature (ν) at$Re_c(\nu) + 200$. This results show that for ν ¡ 0, disturbances experience a marked amplification, which progressively diminishes as both ν and K_s increase. However, when ν exceeds 0.75, noticeable variations in amplification emerge. Overall, the energy loss profiles from V_{ed} tend to approach zero with rising values of both K_s and ν. It is also evident that none of the curves remain constant across the different height of grooves. This indicates that the influence of wall roughness coupled with temperature-dependent viscosity does not align precisely with the impact of the temperature, as reported by Miller et al. [36] and Al-Malki et al. [37].

As we mentioned regarding the clarification of the components of the equation (4.5). Figure 8(b) shows that the interplay between flow over a rough plate and the two components is examined across different temperature-dependence levels. Increasing groove depth leads to higher energy dissipation, although small oscillations in the energy contribution from V_{ed} become apparent once K_s is greater than zero.

Figure 8(c) illustrates the energy balance calculation for fixed ν at $-0.75, 0, 0.75$, in order, with roughness. In this scenario, the effects of the horizontal or vertical grooves are examined for the energy production term R_{ep}, the energy dissipation V_{ed}, and the total mechanical energy T_{me} of the system. The results indicate that T_{me} significantly decreases as K_s increases, due to a simultaneous reduction in both energy production and energy dissipation with rising K_s and ν. The energy analysis technique using bar charts in Figure 8(c) confirms our interpretation of the results shown in the two Figures 8(a) and (b), which were previously presented using curves.

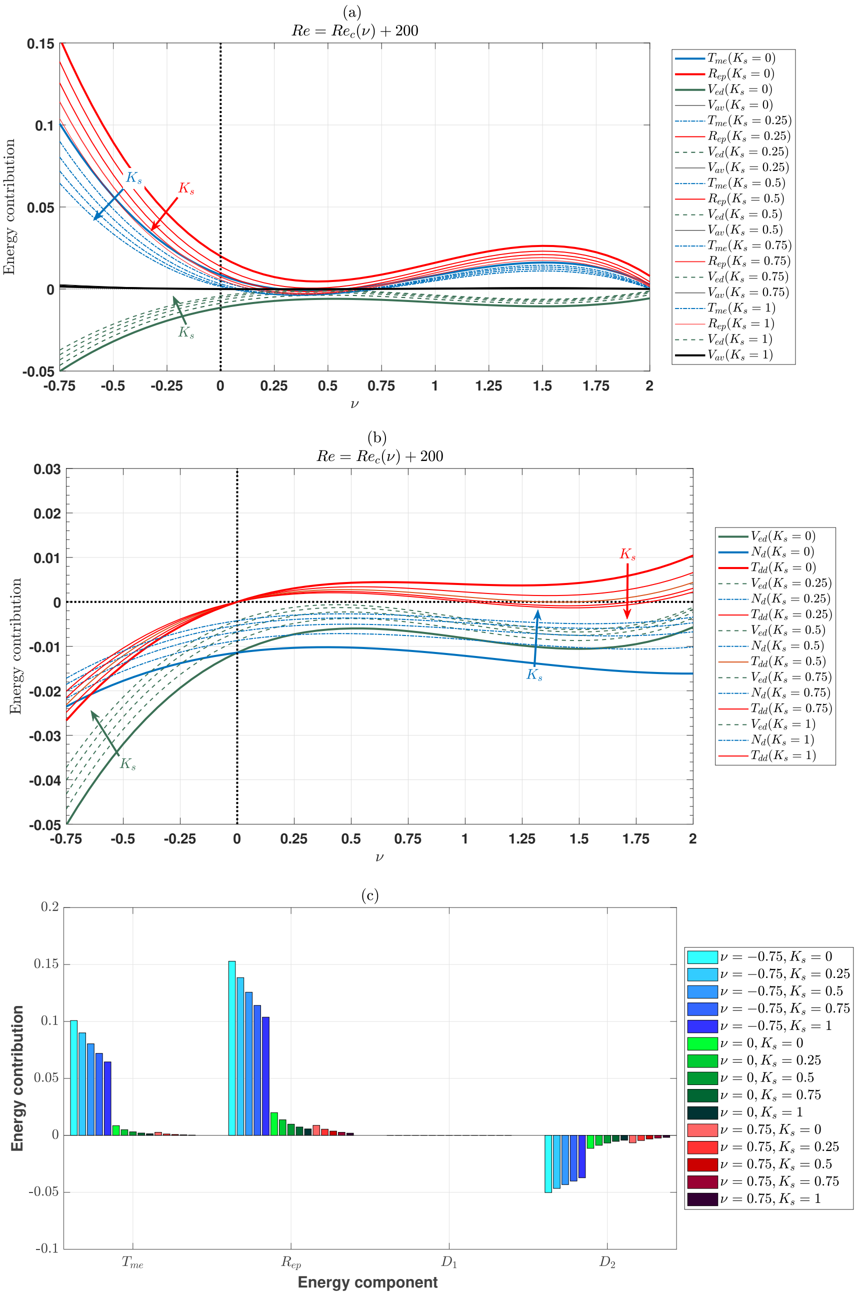

Figure 8: (a) Energy contributions from individual components and (b) overall and individual energy dissipation caused by viscosity, shown across various temperature-dependent scenarios (ν), and K_s. Black dashed lines (—)horizontal and vertical (. . .) serve as reference markers for zero energy input and output, respectively. (c) The outcome of the energy balance integral illustrates how each component contributes to the total energy across different values of grooves intensities, while keeping ν constant at $-0.75, 0, 0.75$. Here, (D_1) and (D_2) represent the first and second terms of the viscous dissipation (V_{ed}).

5. Discussion and Conclusions

A comprehensive linear stability assessment has been conducted on the geometric shape boundary layer in the presence of surface roughness, modeled through the application of slip boundary conditions at the surface wall. In this formulation, partial slip effects were incorporated into the no-penetration conditions of the unperturbed base flow of a fluid whose viscosity depends on temperature. The present analysis evaluates the stability characteristics of the (T-S) instabilities across partial wavy slips on a heated plate corresponding to horizontal or vertical grooves $K_s > 0$.

Integrating this roughness pattern with positive temperatures on uniformly heated plates significantly enhances the stability of the (T–S) instability flows. An energy balance analysis reveals that this substantial stabilizing effect results from a reduction in Reynolds stress energy production, accompanied by an increase in energy loss through viscous dissipation.

These results on the general effect of surface roughness are in complete agreement with previous studies [20], [21], [22], in which the roughness was applied in a manner similar to that used in the current work on the surface of a heated plate. Although previous studies applied the MW model to rotating geometries, the results are in fully agreement.

Smith [38], using the triple-deck framework, argued that the lower deck generates a displacement function that affects the main deck. This displacement exhibits a wave-like structure, arising from the undulating surface below. For sufficiently small roughness heights, the boundary condition can be written as:

$$u^*(0) = m\frac{\partial u^*}{\partial z^*}(0), \quad m = -k\, f(r^*, k),$$

where k is the roughness height and $f(r^*, k)$ represents the surface shape function. When $k = \mathcal{O}(\mathrm{Re}^{-5/8} r^*)$, the lower deck becomes nonlinear, requiring the displacement function to be obtained numerically.

To examine this in more detail, Chicchiero *et al.* [39] compared mean-flow profiles predicted by triple-deck theory (TDT) with those from direct numerical simulations (DNS), the latter incorporating a slight modification of the von Kármán-type flow described by Miklavčič and Wang [19]. They found that for groove wavelengths exceeding 4 and roughness height $k = 0.1$, the time-averaged velocity field became independent of the groove wavelength. The agreement between (TDT) and (DNS) predictions was reported to be strong.

In this study, we adopted the same values of roughness used in previous research, namely 0, 0.25, 0.5, 0.75, and 1. When comparing the effect of these values on the stability of fluid flow, several observations emerge. Although earlier investigations were conducted on rotating geometrical shapes such as disks, where the roughness grooves were arranged concentrically, radially, or symmetrically, the grooving method—whether circular, radial, or a combination of both—resembles, to some extent, the grooving applied on flat plates in either horizontal or vertical orientations. Therefore, it is possible to compare fluid slip at the same values across these types of geometrical configurations.

In prior studies on the rotating disk, the maximum Reynolds number recorded was $Re = (722.6)$ for the cross-flow type of neutral curves under the effect of radial grooves when their value was equal to one, as reported in Cooper's study [20]. Meanwhile, in our current study, the highest Reynolds number ($Re = 944.2$) was obtained under the influence of horizontal or vertical grooves with a value of one. This finding indicates that roughness in the form of parallel grooves enhances the stability of fluid flow over flat plates more effectively than other geometrical shapes.

Our findings were interpreted in the framework of chemical vapor deposition (CVD) reactor flows, where viscosity decreases as temperature rises ($\nu < 0$) and typical operation occurs around $Re \approx 200$. For $\nu \approx -0.62$, representative of dry air in the 300–1300 K range [41], the onset of instability appears below $Re = 200$. At even lower viscosity ($\nu = -0.75$), the flow destabilizes more readily, with a critical Reynolds number of about 150. Surface roughness generally suppresses instabilities, although its stabilizing influence is reduced when $\nu = -0.75$ and $K_s = 1$. For $\nu = -0.62$, increasing K_s from 0 to finite values raises the critical Reynolds number from roughly 150 to above 160, implying that deeper grooves could enhance stability.

A natural extension of this model is to incorporate temperature-dependent density, thereby accounting for thermal expansion, as advocated by Jensen et al. [40]. Because the Prandtl number and specific heat show only minor temperature sensitivity [42], density variations may provide sufficient compensation to justify an incompressible treatment. The Blasius formulation adopted here parallels earlier Poiseuille-based descriptions of metal–organic CVD (MOCVD) reactor flows [43,44]. Still, a complete assessment requires careful inclusion of temperature effects on all transport properties, so that the validity of various approximations can be critically evaluated. Following the approach of Ref. [44], we plan to explicitly incorporate density dependence in future work.

The chemistry underlying CVD is intrinsically complex, consisting of multiple stages and numerous reaction pathways [36]. A rigorous description would therefore require solving a full set of coupled species-continuity equations. However, since reactant concentrations are generally small compared to those of the carrier gas, it is often adequate to employ a simplified formulation based on a single diffusion equation that neglects homogeneous gas-phase reactions [34]. Even within this reduced framework, cross-species transport driven by thermal gradients can still be represented through the Soret effect [45].

Acknowledgments

The author would like to acknowledge the Deanship of Graduate Studies and Scientific Research, Taif University, for funding this project.

References

1. Cervo, G. D., Mansur, S. S., & Vieira, E. D. R. (2004). Flow over rough surfaces. In *Proceedings of the 22nd International Congress of Mechanical Engineering (COBEM)*, Ribeirão Preto, Brazil.
2. Okajima, A. (1982). Strouhal numbers of rectangular cylinders. *Journal of Fluid Mechanics*, 123, 379–398.
3. Lindquist, C., Mansur, S. S., & Vieira, E. D. R. (1998). Experimental study of the flow around rectangular cylinders: An application to compact heat exchangers. In *Proc. of the 8th Brazilian Congress of Thermal Sciences and Engineering*, Rio de Janeiro, Brazil.
4. Lindquist, C., Mansur, S. S., & Vieira, E. D. R. (2010). Flow around square cylinders in several attack angles. In *Proc. of the 13th Brazilian Congress of Thermal Sciences and Engineering*, Uberlândia, Brazil.
5. Hopf, L. (1923). The measurement of the hydraulic roughness. *Mathematik und Mechanik*, 3, 329–339.
6. Saleh, O. A. B. (2005). *Fully developed turbulent smooth and rough channel and pipe flows* (Ph.D. Thesis, Erlangen-Nürnberg University).
7. Nikuradse, J. (1933). Laws of flow in rough pipes. *NACA Technical Memorandum*, 361.
8. Nikuradse, J. (1950). Laws of flow in rough pipes. *NACA Technical Memorandum TM*, 1292.
9. Colebrook, C. F., & White, C. M. (1937). Experiments with fluid friction in roughened pipes. *Proceedings of the Royal Society of London. Series A*, 906, 367–381.
10. Moody, L. F. (1944). Friction factors for pipe flow. *Transactions of the American Society of Mechanical Engineers*, 66, 671–684.
11. Jiménez, J. (2004). Turbulent flows over rough walls. *Annual Review of Fluid Mechanics*, 36, 173–196.
12. Perry, A. E., Schofield, W. H., & Joubert, P. N. (1969). Rough wall turbulent boundary layers. *Journal of Fluid Mechanics*, 2, 383–413.
13. Schultz, M. P., & Flack, K. A. (2007). Rough wall turbulent boundary layers. *Journal of Fluid Mechanics*, 580, 381–405.
14. Flack, K. A., & Schultz, M. P. (2007). Examination of a critical roughness height for outer layer similarity. *Physics of Fluids*, 9, 095104.
15. Squire, D. T.; Morrill-Winter, C.; Hutchins, N.; and Chong, M. S. Comparison of turbulent boundary layers over smooth and rough surfaces up to high Reynolds numbers. *Journal of Fluid Mechanics*, 2016, **795**, 210–248.
16. Sareen, A. (2012). *Drag reduction using riblet film applied to airfoils for wind turbines* (Ph.D. Thesis, University of Illinois at Urbana-Champaign).
17. Bhaganagar, K., & Kim, J. (2006). Direct numerical simulation of turbulent boundary layer over a rough wall. *Physics of Fluids*, 18, 025102.
18. Molki, M., Fahri, M., & Ozbay, O. (1993). A new correlation for pressure drop in arrays of rectangular blocks in air cooled electronic units. *ASME HTD*, 237, 75–81.
19. Miklavčič, M., & Wang, C. Y. (2004). The flow due to a rough rotating disk. *Zeitschrift für Angewandte Mathematik und Physik ZAMP*, 55, 235–246.

20. Cooper, A. J., Harris, J. H., Garrett, S. J., Özkan, M., & Thomas, P. J. (2015). The effect of anisotropic and isotropic roughness on the convective stability of the rotating disk boundary layer. *Physics of Fluids*, 27, 014107.

21. Al-Malki, M. A. S., Garrett, S. J., Camarri, S., & Hussain, Z. (2021). The effects of roughness levels on the instability of the boundary-layer flow over a rotating disk with an enforced axial flow. *Physics of Fluids*, 33, 104109.

22. Al-Malki, M. A. S., Fildes, M., & Hussain, Z. (2022). Competing roughness effects on the non-stationary crossflow instability of the boundary-layer over a rotating broad cone. *Physics of Fluids*, 34, 104103.

23. Blasius, H. (1907). *Grenzschichten in Flüssigkeiten mit kleiner Reibung*. Druck von BG Teubner.

24. Tollmien, W. (1929). Über die Entstehung der Turbulenz. *Nachr. Ges. Wiss. Göttingen Math.-Phys. Kl II*, 21.

25. Schlichting, V. H. (1933). Laminare Strahlausbreitung. *ZAMM*, 13(4), 260–263.

26. Schubauer, G. B., & Skramstad, H. K. (1947). Laminar boundary-layer oscillations and stability of laminar flow. *Journal of the Aeronautical Sciences*, 14(2), 69–78.

27. Fasel, H., & Konzelmann, U. (1990). Non-parallel stability of a flat-plate boundary layer using the complete Navier-Stokes equations. *Journal of Fluid Mechanics*, 221, 311–347.

28. Jordinson, R. (1970). The flat plate boundary layer. Part 1. Numerical integration of the Orr-Sommerfeld equation. *Journal of Fluid Mechanics*, 43(4), 801–811.

29. Smith, F. T. (1979). On the non-parallel flow stability of the Blasius boundary layer. *Proceedings of the Royal Society A*, 366(1724), 91–109.

30. Gaster, M. (1974). On the effects of boundary-layer growth on flow stability. *Journal of Fluid Mechanics*, 66(3), 465–480.

31. Chomaz, J. M. (2005). Global instabilities in spatially developing flows: Non-normality and nonlinearity. *Annual Review of Fluid Mechanics*, 37(1), 357–392.

32. Van Ingen, J. The e^{N} method for transition prediction: Historical review of work at TU Delft. In *Proceedings of the 38th Fluid Dynamics Conference and Exhibit*, 2008, p. 3830.

33. Bertolotti, F. P., Herbert, T., & Spalart, P. R. (1992). Linear and nonlinear stability of the Blasius boundary layer. *Journal of Fluid Mechanics*, 242, 441–474.

34. Holstein, W. L. (1992). Design and modeling of chemical vapor deposition reactors. *Progress in Crystal Growth and Characterization of Materials*, 24(2), 111–211.

35. Kafoussias, N. G., & Williams, E. W. (1995). The effect of temperature-dependent viscosity on free-forced convective laminar boundary layer flow past a vertical isothermal flat plate. *Acta Mechanica*, 110, 123–137.

36. Miller, R., Garrett, S. J., Griffiths, P. T., & Hussain, Z. (2018). Stability of the Blasius boundary layer over a heated plate in a temperature-dependent viscosity flow. *Physical Review Fluids*, 3(11), 113902.

37. Al-Malki, M., Hussain, Z., Garrett, S., & Calabretto, S. (2021). Effects of parietal suction and injection on the stability of the Blasius boundary-layer flow over a permeable, heated plate. *Physical Review Fluids*, 6(11), 113902.

38. F. T. Smith, "Laminar flow over a small hump on a flat plate," *Journal of Fluid Mechanics*, vol. 57, pp. 803–824, 1973.

39. C. Chicchiero, A. Segalini, and S. Camarri, "Triple-deck analysis of the steady flow over a rotating disk with surface roughness," *Physical Review Fluids*, vol. 6, 014103, 2021.

40. A. Jensen, B. Smith, and C. Clark, "Modeling of CVD reactors," *Journal of Fluid Mechanics*, vol. 123, pp. 45–67, 2019.

41. Engineering Toolbox, "Dry air properties," Available at: `https://www.engineeringtoolbox.com/dry-air-properties-d-973.html`.

42. W. M. Kays and M. E. Crawford, *Convective Heat and Mass Transfer*, 3rd ed., McGraw-Hill, 1993.

43. J. V. D. Ven, G. M. J. Rutten, M. J. Raaijmakers, and L. J. Giling, "Gas phase depletion and flow dynamics in horizontal MOCVD reactors," *J. Cryst. Growth*, vol. 76, pp. 352, 1986.

44. P.-Y. Lagrée, "Thermal mixed convection induced locally by a step change in surface temperature in a Poiseuille flow in the framework of Triple Deck theory," *Int. J. Heat Mass Transf.*, vol. 31, pp. 2509, 1999.

45. J. K. Platten, "The Soret effect: A review of recent experimental results," *Journal of Applied Mechanics*, vol. 73, p. 5, 2006.

Department of Mathematics and Statistics,
Faculty of Science, Taif University,
P.O. Box 11099, Taif 21944, Saudi Arabia.
E-mail address: `m.malky@tu.edu.sa`